








Deep Learning Approach to the Texture Optimization Problem for Friction Control in Lubricated Contacts

Alexandre Silva ^{1,2}, Veniero Lenzi ^{1,2,*}, Sergey Pyrlin ^{1,2}, Sandra Carvalho ³,
Albano Cavaleiro ³ and Luís Marques ^{1,2}

¹Physics Center of the Universities of Minho and Porto (CF-UM-UP), University of Minho, Campus de Gualtar, 4710-057, Braga, Portugal

²Laboratory of Physics for Materials and Emergent Technologies, LapMET, University of Minho, 4710-057 Braga, Portugal

³CEMMPRE – Centre for Mechanical Engineering Materials and Processes, Department of Mechanical Engineering, University of Coimbra, Rua Luís Reis Santos, 3030-788, Coimbra, Portugal

 (Received 4 January 2023; revised 7 March 2023; accepted 25 April 2023; published 24 May 2023)

The possibility to control friction through surface microtexturing can offer invaluable advantages in many fields, from wear and pollution reduction in the transportation industry to improved adhesion and grip. Unfortunately, the texture optimization problem is very hard to solve using traditional experimental and numerical methods, due to the complexity of the texture configuration space. Here, we apply machine learning techniques to perform the texture optimization, by training a deep neural network to predict, with extremely high accuracy and speed, the Stribeck curve of a textured surface in lubricated contact. The deep neural network is used to completely resolve the mapping between textures and Stribeck curves, enabling a simple method to solve the texture optimization problem. This work demonstrates the potential of machine learning techniques in texture optimization for friction control in lubricated contacts.

DOI: [10.1103/PhysRevApplied.19.054078](https://doi.org/10.1103/PhysRevApplied.19.054078)

I. INTRODUCTION

Our world is overwhelmed by the environmental impact of human activity, and there is an imperative need to reduce pollution and mitigate its effects to avoid irreversible global warming. The transportation industry, one of the largest contributors to polluting emissions, wastes a significant part of fuel and energy in overcoming friction forces between moving parts in contact [1], meaning that any solution to reduce friction would provide huge environmental and economic benefits. Because of this, research on friction reduction has always been at the forefront of tribology research and many possible solutions exist, such as the application of surface coatings [2] and the use of better performing and more environmentally friendly lubricant formulations [3]. One of the most promising ways to control friction between contacting surfaces is provided by surface texturing, a process that is increasingly more efficient due to significant processing advances [4], allowing for the rapid generation of patterned surfaces. It is well known that the fine control of friction through surface texturing can be achieved in nature. For example, sharks are covered in a regular array of denticles, which help to achieve drag reduction [5]. The same reduction is seen

in the skin of snakes and certain lizards that have developed scales to reduce dry-contact friction [6]. Specific nanohierarchically structured patterns found in the feet of tree toads [7,8] and geckos [9] are shown to provide strong boundary friction, granting them better grip on vertical surfaces. In engineering applications, many different kinds of nature-inspired patterns are also tested for friction control [8].

However, the design of these textures is, in general, based on trial-and-error methods, meaning that the optimal texture for a specific application is extremely hard to find. From an experimental perspective, textured samples need to be fabricated and tested; thus, optimizing a specific pattern would require an extensive sampling of the texture parameter space, resulting in time and resource costs that are prohibitive [10,11]. The same problem occurs when using numerical approaches to evaluate the tribological performance of a system, where the Stribeck curve [12] is calculated by solving the Reynolds equation [13,14], for multiple sliding speeds, coupled with a model for treating contact friction [15]. Even if the simulation process is faster as a whole, when compared to a single experiment, the calculations still require typically minutes to complete, meaning that our ability to sample the possible configuration space is incredibly limited [16]. Moreover, the relationship between patterns and resulting Stribeck curves

*veniero.lenzi@fisica.uminho.pt

is expected to be highly nonlinear, based on current experimental and numerical understanding [4,17–19]. A possible solution to the apparently insurmountable texture optimization problem might be offered by machine learning techniques. Machine learning (ML) encompasses a large range of algorithms and modeling tools used for large data processing tasks [20,21], with typical applications being classification and regression problems in information technology [22,23]. One of the most prominent ML techniques is represented by deep neural networks (DNNs), which are used with considerable success in many fields of physics, from applications in condensed matter [24,25] and materials science [25,26] to the solution of complex nonlinear equations [27,28].

Triboinformatics has recently emerged as a research area combining tribology with big data methods, such as machine learning and artificial intelligence techniques [29–31]. These approaches can help in establishing correlations in tribological data to predict the behavior of materials and provide insights and a broader understanding of the friction and wear mechanisms [32]. A recent example is the development by Almqvist of a physics-informed neural network capable of solving the one-dimensional Reynolds equation [33]. This approach is meshless, thus it solves one of the main bottlenecks in traditional numerical solutions of lubricated contacts, that is, the reliance on a mesh. What makes DNNs particularly appealing for the texture optimization problem is their universal approximation capability [22,23], coupled with their extreme speed when compared with traditional methods [28]. In texture optimization problems, DNNs are used to optimize the features of periodic patterns of nanopillars in optic metamaterials to achieve the desired properties, i.e., high electromagnetic wave absorption in some frequency windows [28]. In these studies, a DNN replaced the Maxwell equation solver, and it can predict, on the millisecond timescale, an absorbance spectrum based solely on the periodic pattern features.

Here, we develop an effective method for the optimization of surface-texturing patterns for friction applications based on a deep neural network. The DNN is designed and trained to accurately predict the Stribeck curve of a dimple-textured surface, thus replacing the standard Reynolds equation solver in the solution of the forward problem. Moreover, to solve the inverse problem, a fast search-based approach is implemented to predict a set of candidate surface parameters (dimple pattern and dimple radius) that yield a set of closely matching Stribeck curves. The performance and accuracy of the DNN and the inverse approach are validated by comparing with the solutions provided by a numerical solver of the Reynolds and contact-friction model equations.

II. METHODS

A. Model for lubricated nonconformal contact of textured surfaces

We consider a parabolic shaped fully lubricated nonconformal contact of total area A similar to a lubricated journal bearing. Let $h_0 \equiv h_0(x, y)$ describe the untextured gap geometry (height profile) between the two surfaces moving in relative motion with speed U , while subject to external load F , as schematically represented in Fig. 1(a). The texturing is introduced by creating a 5×5 grid of cosine square-shaped dimples. The dimple profile heights, h_d , are added to the untextured profile, h_0 , to obtain the total height profile, h (see Sec. 1 of the Supplemental Material [34]).

To obtain the pressure profile, p , within the lubricant, we solve the Reynolds equation, derived from the Navier-Stokes equations [14], after considering the lubricant film to be at constant temperature T , constant density ρ , and constant viscosity μ . Additionally, we do not consider any surface-deformation effects; therefore, the shape of the height profile remains constant throughout the simulations. The influence of the divergent domain on the film density is the possible formation of film rupture caused by cavitation (formation of vapor-filled cavities) [35–38]. To consider this effect, we introduce a system of equations for the pressure, p , and cavitation fraction, θ , profiles:

$$\nabla \cdot (h^3 \nabla p) + 6 \mu U \frac{\partial (h\theta)}{\partial x} = 6 \mu U \frac{\partial h}{\partial x}, \quad (1)$$

$$p\theta = 0, \quad (2)$$

$$p \geq 0, \quad (3)$$

$$\theta \geq 0. \quad (4)$$

The system of Eqs. (1)–(4) represents a linear complementarity problem [39–41], which is solved using the inexact Newton (INE) method [42] by restructuring the system of equations into a damped Newton iteration. The INE method ensures that the solution follows the non-negativity conditions at every iteration, thus providing a correct physical description of cavitation boundaries [16].

Depending on sliding speed, applied load, and viscosity, the system admits three different regimes of lubricated contact: boundary, mixed, and hydrodynamic; these differ in their main friction mechanisms. Here, only the mixed and hydrodynamic regimes are considered, since they occur in the presence of lubricant within the contact, whereas in the boundary regime the surfaces are in direct contact (dry friction). To treat the mixed-contact regime, both the hydrodynamic and asperity contact forces need to be considered in the same model. To this end, we adopt a load-sharing approach [43], where the total friction force results from the combination of the hydrodynamic and contact

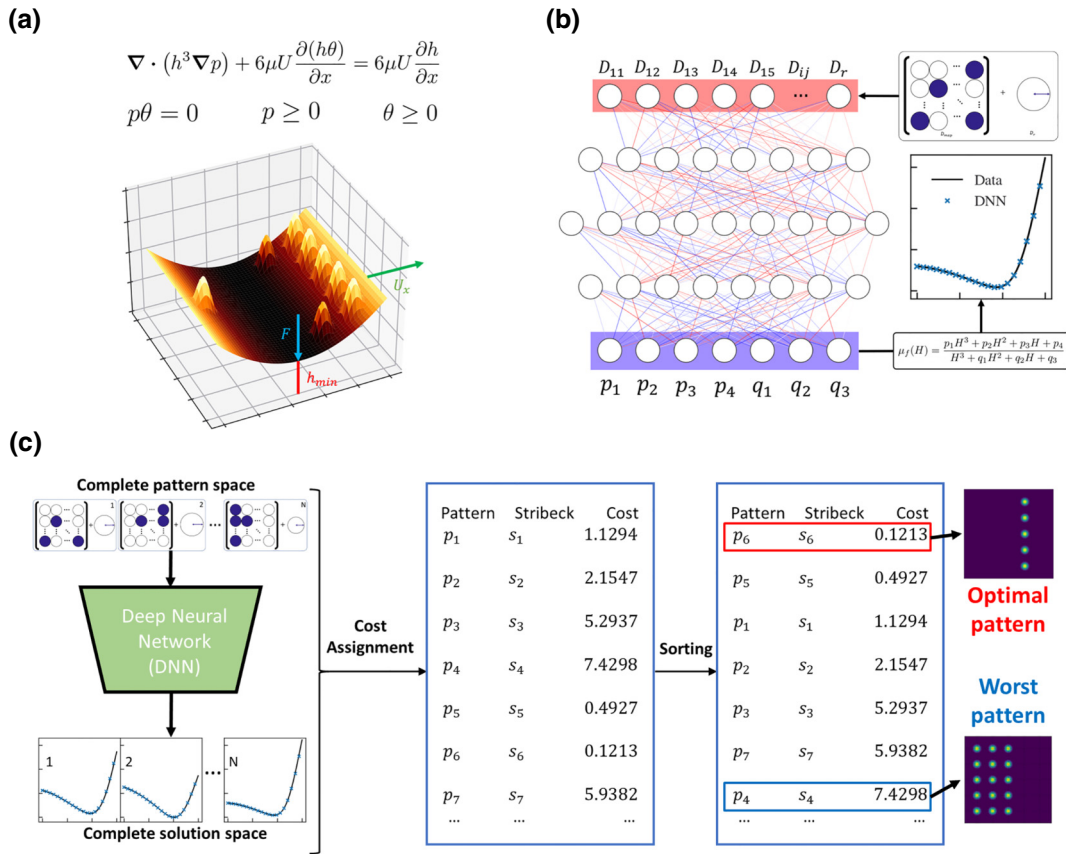


FIG. 1. Schematic representation of the implementation of the DNN solution for the forward and inverse problem in texture optimization. (a) Nonconformal contact of surfaces subject to load F moving relative to each other with speed U , modeled as a height profile function, $h(x, z)$. (b) Machine learning approach to predict the Stribeck curve of a textured surface, defined as the forward problem. (c) Representation of the machine-learning-based algorithm used to solve the texture optimization problem (inverse problem).

terms:

$$f_t = f_{\text{hydro}} + f_{\text{GT}}. \quad (5)$$

The first term, valid only in regions where film rupture does not occur, represents the hydrodynamic component of friction, and depends on the pressure gradient generated within the lubricant film:

$$f_{\text{hydro}} = \left(\frac{h}{2} \frac{\partial p}{\partial x} + \frac{U\mu}{h} \right) A_f, \quad (6)$$

where A_f is the area of the full film domain. The second term of Eq. (5) represents the contact component of friction, that is calculated using the Greenwood-Tripp (GT) contact model [15,44], which considers the roughness of both contacting surfaces. Despite its limitations [45–47] compared with more accurate choices [48], the GT model is adopted here due to its simple computational implementation. Moreover, it is among the most utilized formulations for rough contact and is proven to be robust and efficient at providing a qualitative treatment of friction for design purposes [49].

In the GT model, the total load carried is defined as

$$f_{\text{GT}} = \tau_0 A_a + \mu_{\text{asp}} W_{\text{asp}}, \quad (7)$$

where τ_0 is the Eyring shear stress, A_a is the asperity contact area, W_{asp} is the load carried by asperities in the contacting surfaces, and μ_{asp} is the coefficient of friction of the asperities [49,50]. The load carried by asperities is defined as

$$W_{\text{asp}} = \frac{16\sqrt{2}}{5} \pi (\eta k \sigma)^2 \sqrt{\frac{\sigma}{k}} A E' F_{5/2} \left(\frac{h}{\sigma} \right). \quad (8)$$

The asperity contact area is similarly defined as

$$A_a = \pi^2 (\eta k \sigma)^2 A F_2 \left(\frac{h}{\sigma} \right). \quad (9)$$

The functions $F_{n(m)}(h/\sigma)$ are statistical functions that account for the Gaussian distribution of asperities and can be approximated through a parametric fit [44]. The chosen values of the parameters η , k , and σ present in Eqs. (8) and

(9) reflect the typical values for a well-polished steel surface. It should be noted that this roughness scale is much smaller than characteristic dimple dimensions. A table of numerical values for the parameters used in data generation in the training of the deep neural network is available in Sec. 3 of the Supplemental Material [34].

An open-source finite-element implementation of the solver for the system of Eqs. (1)–(6), FELINE [51], is specifically developed and used to generate the training data and validate the DNN results.

B. Method of solution and Stribeck curve calculation

To obtain the Stribeck curve, one must compute the coefficient of friction (C_f) for each relevant sliding speed as the ratio between the total friction force in Eq. (5) and the total carried load, W , which is calculated from the fluid pressure and the contact [Eq. (8)] terms:

$$C_f(H) = \frac{f_t(H)}{W}, \quad (10)$$

where

$$H = \frac{\mu U}{F} \quad (11)$$

is a dimensionless parameter dependent on the relative sliding speed termed the Hersey number. A total of 50 different Hersey number values, equally spaced on a logarithmic scale, are used for each Stribeck curve in the interval $H \in [10^{-5}, 10^{-2}]$. This is equivalent to a procedure where the relative sliding speed is changed in the interval $U \in [0.043, 43]$ m/s.

For every value of H , C_f is calculated when the total load carried balances the applied load, F . For this purpose, we first perform a solver run with an initial condition for the minimum separation, h_{\min} . The total carried load, W , is then calculated and compared with F , and the minimum separation, h_{\min} , is adjusted by lowering (raising) it if W is smaller (larger) than F . After three iterations, a spline interpolation is used to accelerate convergence, which is reached when $F^{-1}(W - F) < 10^{-3}$.

C. Design and training of the DNN

The textured surface in a lubricated contact is defined by a set of parameters: the dimple map, D_{map} , of dimension (D_x, D_y) , which describes the presence and position of dimples on the surface (see Sec. 1 of the Supplemental Material [34]); the dimple depth, D_d ; the dimple radius, D_r ; the parabolical edge, E_0 ; and the surface-roughness parameters $\eta k \sigma$. The value of dimple depth is fixed to $D_d^0 = 6 \mu\text{m}$ to isolate the influence of dimple radius. This way, the complexity of the optimization problem is greatly reduced, with only one tunable parameter present in addition to the dimple map. Further details regarding the effects

of D_r and D_d on the load-carrying capacity (LCC) and h_{\min} of the textured contacts can be found in the Supplemental Material [34].

Because we consider a 5×5 grid of dimples with six possible D_r values in the interval $[40, 60] \mu\text{m}$, our network input consists of 26 parameters, that is, 25 possible spots for dimple placement represented as Boolean variables and a globally applied value for dimple radius. The D_r interval is selected, since it provides a sufficient range for optimization while remaining within the validity conditions of the Reynolds equation. Even if such configuration space appears simple at first glance, it contains a total of $N = 6 \times 2^{25} \approx 2.01 \times 10^8$ possible texture configurations, rendering the texture optimization problem impossible to solve for any traditional solution approach.

To represent all Stribeck curves in the configuration space with the same number of parameters, we perform a fit of our data calculated with FELINE using a rational polynomial form defined as

$$f_n^m(x) = \frac{p_1 x^n + p_2 x^{n-1} + \dots + p_n x + p_{n-1}}{x^m + q_1 x^{m-1} + \dots + q_{m-1} x + q_m}, \quad (12)$$

with polynomial degrees $(n, m) = (3, 3)$. This rational polynomial is found to be the best compromise between accuracy and total number of parameters when representing a Stribeck curve.

As a result, the DNN output consists of seven rational fit parameters that allow the reconstruction of the Stribeck curve, thus reducing the overall number of output parameters while not significantly affecting precision. This fitting step regularizes the output of the network.

Regarding the DNN architecture, we adopt a simple topology consisting of six fully connected hidden layers with a number of neurons $\{32, 64, 96, 96, 64, 32\}$ under no regularization using the rectified linear unit (RELU) activation function with He normal initialization [52] due to its performance and simplicity [53,54]. Since the number of hidden layers in our network is small and the width of these layers is sufficiently large, we do not expect the “dying RELU problem” in this study [55]. The optimizer of choice is NADAM, as it incorporates Nesterov momentum (with default hyperparameters) and can improve the convergence of the learning process [56–58]. To further optimize the training process, we sample the validation-set loss as a function of learning rate after ten steps of training. This allows us to carefully select a value for the learning rate (10^{-3}). E_{rms} (root-mean-square error) of the predicted rational fit coefficients is used as the network-loss function. The training and testing process is implemented with PYTHON 3.9 using the Keras high-level application program interface [59] of TensorFlow version 2 [60].

The DNN training set is populated by randomly sampling sets of dimple maps, D_{map} , the corresponding patterns of which are solved for all D_r values to obtain the corresponding Stribeck curves. In total, around 60 000 different combinations of patterns and dimple radii are computed using the FELINE solver, which requires 6 days of computation time on 300 simultaneously running processes on Intel(R) Xeon(R) CPU E5-2697 v2 cores. This dataset is standardized according to the StandardScaler utility in the scikit-learn PYTHON package [61].

Because the boundary pressure is the same at $y = 0$ and $y = L$, we expect that a mirror reflection of any pattern over the $y = L/2$ axis does not change the corresponding Stribeck curve. This symmetry is explicitly included in the dataset by assigning the same Stribeck curve both to a pattern and to its reflection. This step is important in enhancing the overall physical accuracy of the DNN, while requiring no additional generation of data. From the generated dataset, we select 10% as a validation set; thus, our resulting training set contains 54 000 pairs of surface parameters and Stribeck curves and accounts for only 0.05% of the total configuration space.

III. RESULTS AND DISCUSSION

A. Solution of the forward problem

The forward problem, schematically represented in Fig. 1(b), is solved and examples of the DNN predictions are shown in Fig. 2 for a few cases in the validation set compared with data produced with the FELINE solver. The median E_{rms} of cases in the validation set is 5.7×10^{-4} , meaning that the network predictions are very accurate and

show no appreciable difference from the Stribeck curves calculated with FELINE.

Figure 3(a) shows a histogram of the E_{rms} distribution for the validation-set predictions of the full Stribeck curve and for two separate regimes of the Stribeck curve, that is, the mixed regime and the hydrodynamic regime. The same analysis is performed on a test set of patterns (~ 4000 samples), and it is verified that the network performs well on an arbitrary set of patterns (see Sec. 4 of the Supplemental Material [34]). To correctly establish boundaries for these regimes, we use the lambda parameter criteria [62]:

$$\lambda = \frac{h_{\text{min}}}{\sigma}, \quad (13)$$

where h_{min} denotes the minimum thickness of the lubricant film (or minimum distance between the contacting films) and σ is one of the surface-roughness parameters. For $\lambda > 3$, the contact regime is said to be hydrodynamic, while the mixed regime occurs for $1 < \lambda < 3$. After taking an average of λ for all curves in the validation set, we find that the averaged value, $H = 0.0015$, represents well the point at which the lubrication regime changes. Therefore, for $H \in [0, 0.0015]$, we have the mixed regime, and for $H \in [0.0015, 0.01]$, we have the hydrodynamic regime.

The corresponding median and 95th and 99th percentiles of the different histograms are reported in Table I. Low E_{rms} values ($< 10^{-3}$) are consistently encountered in all regimes, indicating that the trained DNN is reliable across all data. However, a better accuracy of the DNN in the mixed region is observed, compared with the hydrodynamic region. This is likely to be due to the larger span of C_f values in the hydrodynamic region, for the same

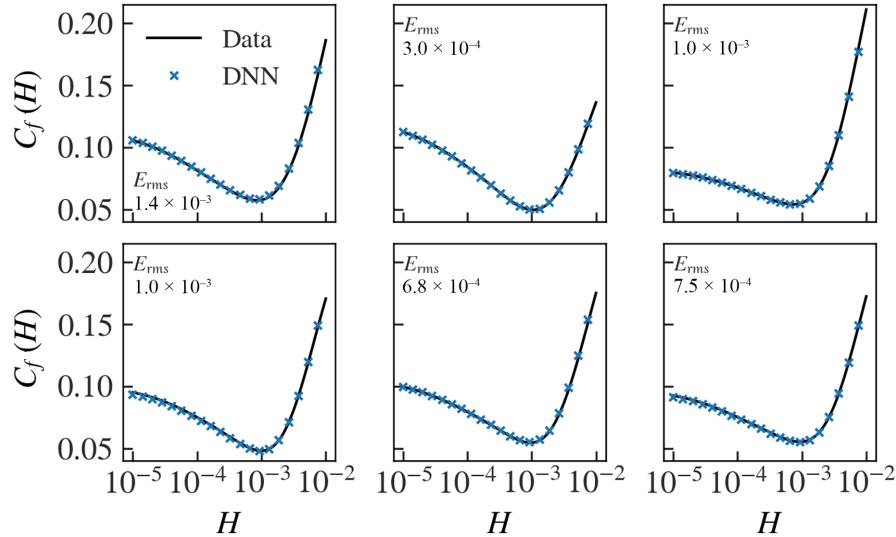


FIG. 2. DNN predictions (crosses) of the Stribeck curves for randomly selected patterns in the validation set. Prediction accuracy is shown in terms of E_{rms} in comparison to the corresponding FELINE solver results (solid lines). DNN results are downsampled for clarity.

TABLE I. Median and 95th and 99th percentiles of the E_{rms} values shown in the histogram in Fig. 3(a).

Regime	Median	99%	95%
Mixed	2.4×10^{-4}	7.9×10^{-4}	6.0×10^{-4}
Hydrodynamic	9.4×10^{-4}	6.1×10^{-3}	3.8×10^{-3}
Total	5.7×10^{-4}	3.4×10^{-3}	2.1×10^{-3}

number of training samples, resulting in a lower-accuracy prediction of the DNN therein.

To assess the quality of the trained network, it is also important to verify its ability to interpolate and extrapolate results in terms of the dimple radius, since it is trained only with six possibilities. In this regard, we compare both the network and the FELINE solver solutions for values between and outside the dimple-radius interval of 40–60 μm .

A pattern is randomly picked and its corresponding Stribeck curve is computed with the DNN and FELINE to obtain an E_{rms} of their difference, which is plotted in Fig. 3(b) as a function of D_r . As one can see in Fig. 3(b), in region II, the interpolation region, there is a small difference between the interpolation results from the DNN and the corresponding ones from the FELINE solver, showing that the network is capable of accurate interpolating behavior.

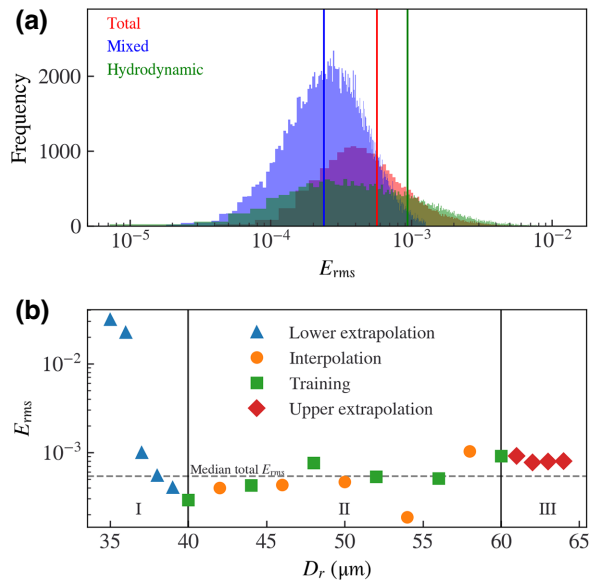


FIG. 3. (a) Histogram of E_{rms} for all patterns in the validation set in different regimes. Medians for the mixed, hydrodynamic, and total regions are also shown. (b) Interpolation and extrapolation study of dimple radius versus E_{rms} where (I) indicates the lower extrapolation bound, $D_r \in [35, 39]$; (II) indicates the interpolated values, $D_r \in [42, 46, 50, 54, 58]$, and values used in training; and (III) indicates the upper extrapolation bound, $D_r \in [61, 65]$.

For the extrapolation cases, regions II and III, we see that the lower extrapolation bound works significantly worse than the upper extrapolation bound. In the hydrodynamic regime of lubrication, C_f increases linearly with increasing Hersey number. Contrary to this, in the mixed regime of lubrication, C_f increases exponentially with decreasing Hersey number. Extrapolation is typically more accurate for linear behavior, hence resulting in a larger extrapolation error for the lower bound of extrapolation.

In terms of timing, the DNN is 10^6 times faster when compared with the FELINE solver. In conclusion, we successfully design a DNN that meets the requirements of speed and accuracy needed to fully solve the texture optimization problem for tribological applications.

B. Solution of the inverse problem

The inverse problem, schematically represented in Fig. 1(c), consists of the ability to predict optimal patterns starting from desired characteristics of a particular system. With our capable forward-problem DNN solver, it is possible to obtain the Stribeck curve for every case in the full configuration space defined by 25 possible dimples and six possible radii, that is, a total of about 3.3×10^8 cases. Let (p_k, s_k) stand for the k th pattern and Stribeck pair in the configuration space and consider a value, or cost, $C \equiv C(p_k, s_k)$, that we can assign to each pair, such

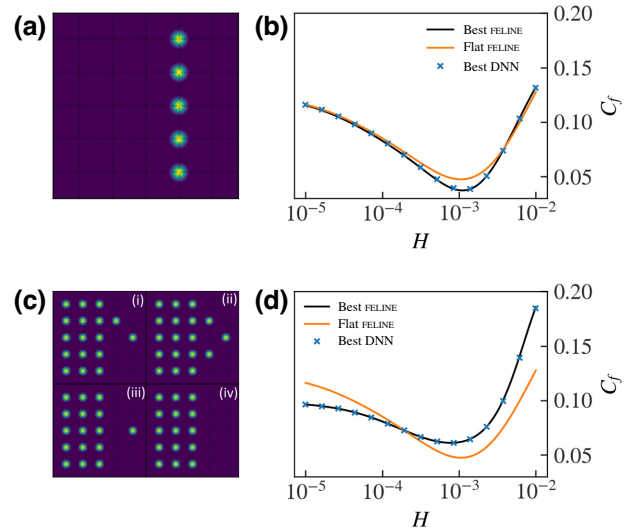


FIG. 4. Resulting patterns and Stribeck curves from the cost assignment and sorting method used to find the optimal friction reducing (increasing) patterns in the mixed regime. (a) Optimal pattern that yields the Stribeck curve with the smallest minimum. (b) Corresponding Stribeck curves calculated with both FELINE and the DNN and compared with the untextured case. (c) Family of textures that yield nearly matching Stribeck curves with the largest C_f minimum. (d) Stribeck curves of pattern (i) calculated with both FELINE and the DNN and compared with the untextured case. DNN results (crosses) are downsampled for clarity.

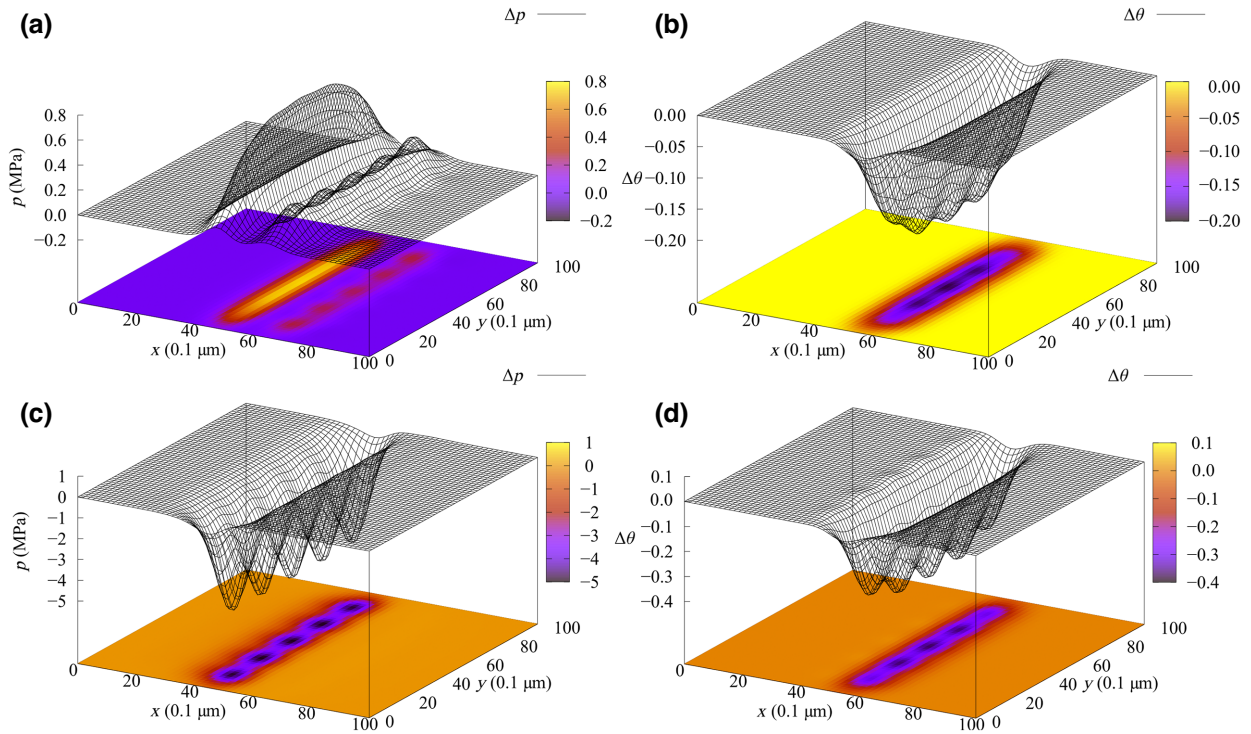


FIG. 5. Pressure and cavitation profiles, determined at the Hersey number of the C_f minimum of the untextured Stribeck curve for the optimal pattern in Fig. 4(a) for friction reduction and for friction gain in Fig. 4(c). (a) Pressure difference between untextured and textured cases in Fig. 4(a). (b) Cavitation difference between untextured and textured cases in Fig. 4(a). (c) Pressure difference between untextured and textured cases in Fig. 4(c). (d) Cavitation difference between untextured and textured cases in Fig. 4(c).

as the minimum of the Stribeck curve, s_k . By sorting the list of possible cases by their cost, we obtain the cases with smallest C_f minimum and highest C_f minimum at the top and bottom of the list, respectively. The simple and straightforward algorithm Quicksort [63] is employed for this task.

The resulting optimal pattern for obtaining the smallest C_f minimum using this method is shown in Fig. 4(a), and the corresponding Stribeck curve (solved with both FELINE and the DNN) is also reported in Fig. 4(b), compared with the untextured case. We observe that, in this case, the dimples are present only in a small region right after h_{\min} . The pressure and cavitation profiles of the contact obtained using FELINE, for the predicted optimal texture at the lowest friction point in the Stribeck curve are reported in Figs. 5(a) and 5(b), respectively. We observe an increase in pressure in the convergent gap and a smaller pressure increase in the divergent gap. Furthermore, a significant drop in the cavitation profile leads to an overall reduction of the size of the cavitation region in the divergent gap. The presence of dimples right after the h_{\min} zone appears to hinder the formation of the cavitation region. Thus, the optimal pattern results in smaller film-rupture areas and larger pressures in the convergent area.

Configuration space sorting also allows us to find the pattern that yields the largest C_f minimum. We find a

family of very similar patterns that generate almost indistinguishable Stribeck curves, as shown in Figs. 4(c) and 4(d). In this case, the convergent region of the contact is fully textured, including the h_{\min} area. By looking at the pressure profile [Fig. 5(c)], we observe a significant pressure drop in the convergent gap. This is caused by the presence of dimples in a region that produces most of the

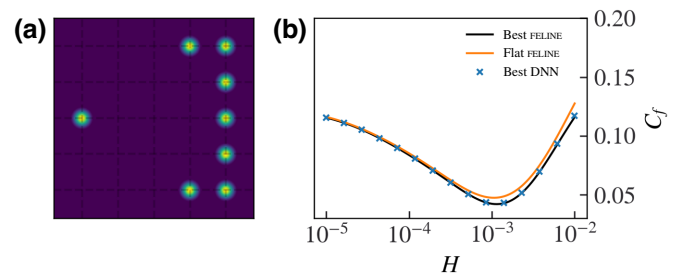


FIG. 6. Resulting pattern and Stribeck curves from the cost assignment and sorting method used to find the optimal friction-reducing pattern in the hydrodynamic regime. (a) Optimal pattern that yields the Stribeck curve with the overall smallest C_f minimum in the hydrodynamic regime. (b) Corresponding Stribeck curves calculated with both FELINE and the DNN are compared with the untextured case. DNN result (crosses) is downsampled for clarity.

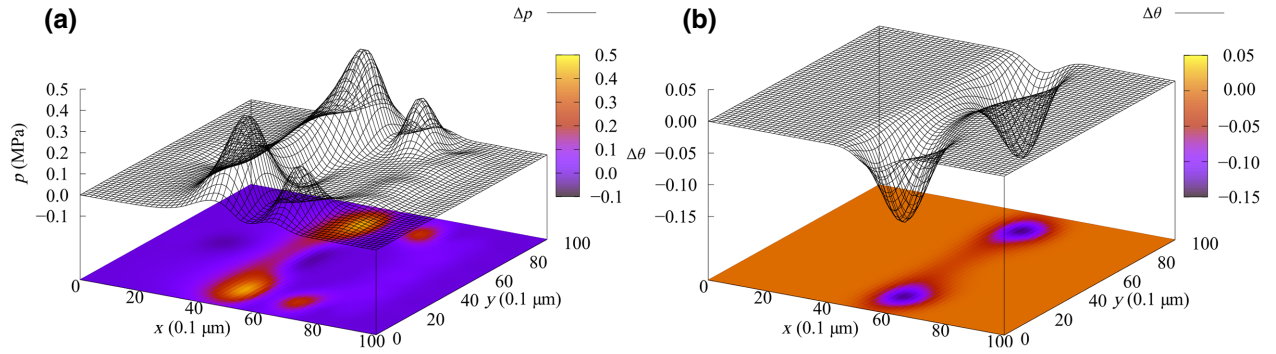


FIG. 7. Pressure and cavitation profiles determined at the Hersey number of the C_f minimum of the untextured case Stribeck curve for the optimal pattern for friction reduction. (a) Pressure difference between the untextured and textured cases. (b) Cavitation difference between the untextured and textured cases.

hydrostatic pressure which counters the applied load. Such simple placement disrupts the pressure profile. The cavitation profile [Fig. 5(d)] also displays a decrease in magnitude, but the total cavitation area is not affected by this.

Curiously, the two families of patterns that provide a significant decrease [Fig. 4(a)] and increase [Fig. 4(c)] in C_f , were already observed and described by Tala-Ighil and co-workers [64]. The reasoning behind the friction increase (decrease) phenomenon described by Tala-Ighil and co-workers accurately matches the observations of our own neural network predictions and further investigation with FELINE. This fact demonstrates that our solution of the inverse problem is capable of correctly identifying the optimal texturing pattern. In terms of accuracy, the DNN solutions are basically indiscernible from the FELINE ones.

The collection of similar patterns (i)–(iv) shown in Fig. 4(c) exemplifies an important feature of a method like

this, which is the ability to find nearly identical solutions generated by different patterns. This is extremely important from an experimental point of view because, at parity of performance, a particular texture may be better in terms of manufacturing cost and speed in a laboratory.

To further test our inverse problem solver, we look for a pattern that reduces friction in the hydrodynamic regime. To achieve this, we define a more elaborate form of the cost:

$$C(p_k, s_k) = \int_{H_1}^{H_2} [s_k(H) - s_0(H)] dH, \quad (14)$$

where H_1, H_2 encompass the hydrodynamic range. This function computes the area under the Stribeck curve in the hydrodynamic region for some Stribeck curve, $s_k \in L$,

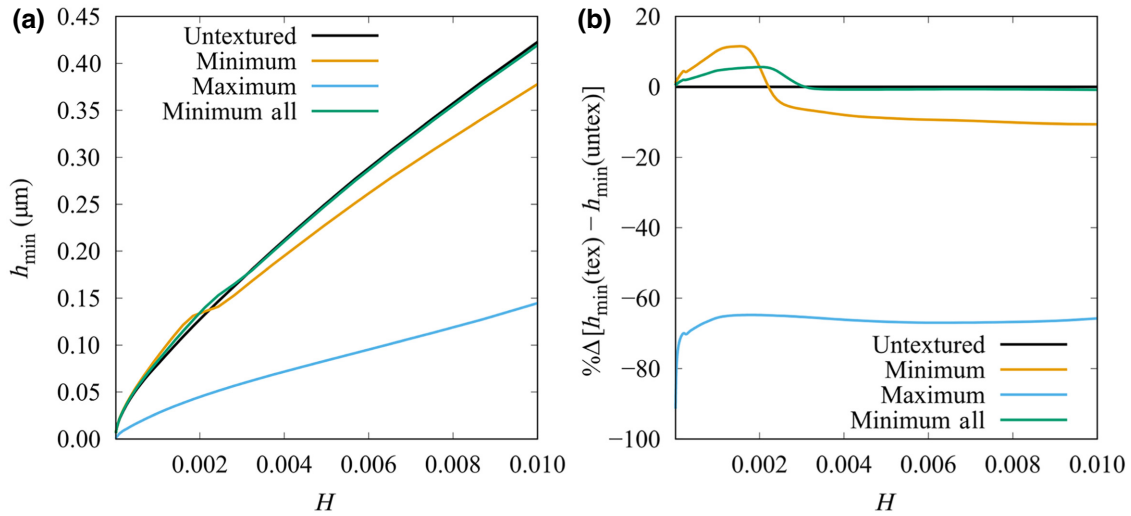


FIG. 8. Effect of texturing on the minimum film thickness as a function of the Hersey number. (a) Comparison between the untextured case and the three cases determined by the neural network, where minimum is the texture of Fig. 4(a), maximum is the texture of Fig. 4(c)(i), and minimum all is the texture of Fig. 6(a). (b) Percentage deviation of the difference in h_{\min} with respect to the untextured case.

minus the area under the Stribeck curve of the untextured case, s_0 . The lowest value of C should correspond to the pattern that maximizes the reduction of C_f in the hydrodynamic regime.

The resulting optimal pattern for maximizing the reduction of C_f in the hydrodynamic regime using this method is shown in Fig. 6(a), and the corresponding Stribeck curve (solved with both FELINE and the DNN) is also reported in Fig. 6(b), compared with the untextured case. The corresponding pressure and cavitation profile differences from the untextured cases are reported in Figs. 7(a) and 7(b), respectively. It is possible to observe an increase of pressure in the convergent and divergent gaps [Fig. 7(a)]. Concerning cavitation, only a slight reduction of the size of the cavitation region in the divergent gap is observed.

The absolute values of h_{\min} and the percentage deviations in the difference of h_{\min} relative to the untextured case for the optimal texture cases for friction reduction (gain) are represented, respectively, in Figs. 8(a) and 8(b). For the optimal texture for friction reduction in the mixed regime (orange line in Fig. 8), about 12% increase in h_{\min} in the mixed regime and about 10% decrease of h_{\min} at larger H numbers are observed. Additionally, for the mixed regime, calculations also show about 5% increase in the LCC coupled with about 22% decrease in the overall cavitation-region area, resulting in a smaller C_f for these sliding speeds. For the optimal texture for friction gain (cyan line in Fig. 8), an 80%–90% decrease in h_{\min} in the mixed regime is observed, stabilizing at around 60% decrease at larger H numbers. Concerning LCC and cavitation area, 33% decrease and no change in the overall cavitation region are found; this explains the significant increase in C_f for this pattern. Finally, for the optimal texture for friction reduction in all regimes (green line in Fig. 8), about 5% increase in h_{\min} in the mixed regime is observed, while no appreciable variation can be seen at larger H numbers. About 3% increase in the LCC, coupled with about 16% decrease in overall cavitation-region area, shows a similar performance to that of the Fig. 4(a) pattern. The combination of these effects results in a slight decrease of C_f for nearly all sliding speeds. Textures that are capable of an effective reduction of friction and an increase in LCC can significantly contribute to extending the service life of the lubricated contact.

The above optimal textures and, in particular, those in Figs. 4(a) and 4(c) clearly demonstrate the capability of our approach for texture optimization problems. In fact, the solution of the inverse problem for the lowest and highest C_f values returns the expected optimal textures [64]. The strength of this method is that the proposed solutions are actually the best ones, since all of the possible configuration space is explored. This demonstrates how the texture optimization problem turns into a very simple task using a DNN to solve the forward problem, which allows

for a very efficient solution of the texture configuration space.

IV. CONCLUSIONS

We successfully design and train a deep neural network capable of accurately predicting the resulting Stribeck curve generated by a dimpled texture with median root-mean-square errors of 5.7×10^{-4} . This type of texture, composed of an array of 5×5 possible dimples with dimple radius D_r , has an unpredictable and highly nonlinear effect on the surface-friction coefficient. The DNN can efficiently compute all possible cases of a total of around 300 million possibilities, trained with only 0.05% of them, thus enabling us to solve the texture optimization problem, which is otherwise impossible to treat with traditional experimental and numerical methods. We determine both extremes of an optimization problem by taking advantage of the incredible performance of our DNN, predicting the relevant optimal textures in the process. We investigate the properties of the developed DNN, such as accuracy, extrapolation, and interpolation capabilities, demonstrating its robustness and reliability. This work paves the way for the use of deep learning as a tool to realize careful friction control of surfaces through optimally designed textures.

The datasets used in this work (training, validation, test datasets, and DNN implementation) are available free of charge from Ref. [65].

ACKNOWLEDGMENTS

This work is supported by the Portuguese Foundation for Science and Technology (FCT, I.P.) in the framework of strategic funding (Grant No. UIDB/04650/2020), Project No. PTDC/EME-SIS/30446/2017. The Advanced Computing Project No. CPCA/A2/4513/2020 is used to access MACC-BOB HPC resources.

The authors have no competing interests to declare that are relevant to the content of this article.

-
- [1] K. Holmberg, P. Andersson, and A. Erdemir, Global energy consumption due to friction in passenger cars, *Tribol. Int.* **47**, 221 (2012).
 - [2] N. Shaigan, W. Qu, D. G. Ivey, and W. Chen, A review of recent progress in coatings, surface modifications and alloy developments for solid oxide fuel cell ferritic stainless steel interconnects, *J. Power Sources* **195**, 1529 (2010).
 - [3] A. E. Somers, P. C. Howlett, D. R. MacFarlane, and M. Forsyth, A review of ionic liquid lubricants, *Lubricants* **1**, 1 (2013).

- [4] I. Etsion, State of the art in laser surface texturing, *J. Tribol.* **127**, 248 (2005).
- [5] G. Liu, Z. Yuan, Z. Qiu, S. Feng, Y. Xie, D. Leng, and X. Tian, A brief review of bio-inspired surface technology and application toward underwater drag reduction, *Ocean Eng.* **199**, 106962 (2020).
- [6] C. Greiner and M. Schäfer, Bio-inspired scale-like surface textures and their tribological properties, *Bioinspiration Biomimetics* **10**, 044001 (2015).
- [7] T. Endlein, A. Ji, D. Samuel, N. Yao, Z. Wang, W. J. P. Barnes, W. Federle, M. Kappl, and Z. Dai, Sticking like sticky tape: Tree frogs use friction forces to enhance attachment on overhanging surfaces, *J. R. Soc., Interface* **10**, 20120838 (2013).
- [8] L. Zhang, H. Chen, Y. Guo, Y. Wang, Y. Jiang, D. Zhang, L. Ma, J. Luo, and L. Jiang, Micro–nano hierarchical structure enhanced strong wet friction surface inspired by tree frogs, *Adv. Sci.* **7**, 2001125 (2020).
- [9] A. Y. Stark, I. Badge, N. A. Wucinich, T. W. Sullivan, P. H. Niewiarowski, and A. Dhinojwala, Surface wettability plays a significant role in gecko adhesion underwater, *Proc. Natl. Acad. Sci. U. S. A.* **110**, 6340 (2013).
- [10] M. Marian, A. Almqvist, A. Rosenkranz, and M. Filion, Numerical micro-texture optimization for lubricated contacts—a critical discussion, *Friction* **10**, 1772 (2022).
- [11] N. K. Myshkin, M. I. Petrokovets, and A. V. Kovalev, Tribology of polymers: Adhesion, friction, wear, and mass-transfer, *Tribol. Int.* **38**, 910 (2005).
- [12] R. Stribeck, *Kugellager Für Beliebige Belastungen* (Springer, Berlin, Germany, 1901).
- [13] A. Akchurin, R. Bosman, P. M. Lugt, and M. van Drogen, On a model for the prediction of the friction coefficient in mixed lubrication based on a load-sharing concept with measured surface roughness, *Tribol. Lett.* **59**, 19 (2015).
- [14] O. Reynolds, IV. On the theory of lubrication and its application to Mr. Beauchamp Tower’s experiments, including an experimental determination of the viscosity of olive oil, *Philos. Trans. R. Soc. London* **177**, 157 (1886).
- [15] J. A. Greenwood and J. H. Tripp, The contact of two nominally flat rough surfaces, *Proc. Inst. Mech. Eng.* **185**, 625 (1970).
- [16] D. Gropper, L. Wang, and T. J. Harvey, Hydrodynamic lubrication of textured surfaces: A review of modeling techniques and key findings, *Tribol. Int.* **94**, 509 (2016).
- [17] C. Greiner, T. Merz, D. Braun, A. Codrignani, and F. Magagnato, Optimum dimple diameter for friction reduction with laser surface texturing: The effect of velocity gradient, *Surf. Topogr.: Metrol. Prop.* **3**, 044001 (2015).
- [18] R. Ausas, P. Ragot, J. Leiva, M. Jai, G. Bayada, and G. C. Buscaglia, The impact of the cavitation model in the analysis of microtextured lubricated journal bearings, *J. Tribol.* **129**, 868 (2007).
- [19] R. F. Ausas, M. Jai, and G. C. Buscaglia, A mass-conserving algorithm for dynamical lubrication problems with cavitation, *J. Tribol.* **131**, 031702 (2009).
- [20] G. Carleo, I. Cirac, K. Cranmer, L. Daudet, M. Schuld, N. Tishby, L. Vogt-Maranto, and L. Zdeborová, Machine learning and the physical sciences, *Rev. Mod. Phys.* **91**, 045002 (2019).
- [21] M. Biehl and A. Mietzner, Statistical mechanics of unsupervised learning, *Europhys. Lett.* **24**, 421 (1993).
- [22] K. Hornik, M. Stinchcombe, and H. White, Multilayer feedforward networks are universal approximators, *Neural Networks*. **2**, 359 (1989).
- [23] G. Cybenko, Approximation by superpositions of a sigmoidal function, *Math. Control Signals Syst.* **2**, 303 (1989).
- [24] J. Carrasquilla and R. G. Melko, Machine learning phases of matter, *Nat. Phys.* **13**, 5 (2017).
- [25] A. J. Lew, C.-H. Yu, Y.-C. Hsu, and M. J. Buehler, Deep learning model to predict fracture mechanisms of graphene, *Npj 2D Mater. Appl.* **5**, 1 (2021).
- [26] K. Guo, Z. Yang, C.-H. Yu, and M. J. Buehler, Artificial intelligence and machine learning in design of mechanical materials, *Mater. Horiz.* **8**, 1153 (2021).
- [27] J. Pathak, B. Hunt, M. Girvan, Z. Lu, and E. Ott, Model-Free Prediction of Large Spatiotemporally Chaotic Systems from Data: A Reservoir Computing Approach, *Phys. Rev. Lett.* **120**, 024102 (2018).
- [28] C. C. Nadell, B. Huang, J. M. Malof, and W. J. Padilla, Deep learning for accelerated all-dielectric metasurface design, *Opt. Express* **27**, 27523 (2019).
- [29] I. Argatov, Artificial neural networks (ANNs) as a novel modeling technique in tribology, *Front. Mech. Eng.* **5** (2019).
- [30] M. Marian and S. Tregel, Current trends and applications of machine learning in tribology—a review, *Lubricants* **9**, 9 (2021).
- [31] Z. Zhang, N. Yin, S. Chen, and C. Liu, Tribo-informatics: Concept, architecture, and case study, *Friction* **9**, 642 (2021).
- [32] Y. Meng, J. Xu, Z. Jin, B. Prakash, and Y. Hu, A review of recent advances in tribology, *Friction* **8**, 221 (2020).
- [33] A. Almqvist, Fundamentals of physics-informed neural networks applied to solve the Reynolds boundary value problem, *Lubricants* **9**, 8 (2021).
- [34] See the Supplemental Material at <http://link.aps.org/supplemental/10.1103/PhysRevApplied.19.054078> for an in-depth discussion of the lubricated contact geometry and dynamics and the neural network training parameters.
- [35] H. G. Elrod and M. L. Adams, A computer program for cavitation and starvation problems, Leeds-Lyon Symp. Tribol. **1st**, 37 (1975).
- [36] B. Jakobsson and L. Floberg, The Finite Journal Bearing, Considering Vaporization: (Das Gleitlager von Endlicher Breite Mit Verdampfung). (1957).
- [37] A. Almqvist, P. Wall, A. Almqvist, and P. Wall, *Modelling Cavitation in (Elasto)Hydrodynamic Lubrication* (IntechOpen, London, UK, 2016).
- [38] M. Giacomini, M. T. Fowell, D. Dini, and A. Strozzi, A mass-conserving complementarity formulation to study lubricant films in the presence of cavitation, *J. Tribol.* **132**, 041702 (2010).
- [39] R. W. Cottle, J.-S. Pang, and R. E. Stone, *The Linear Complementarity Problem* (Society for Industrial and Applied Mathematics, Philadelphia, PA, USA, 2009).

- [40] A. Almqvist, J. Fabricius, R. Larsson, and P. Wall, A new approach for studying cavitation in lubrication, *J. Tribol.* **136**, 011706 (2013).
- [41] L. Bertocchi, D. Dini, M. Giacomini, M. T. Fowell, and A. Baldini, Fluid film lubrication in the presence of cavitation: A mass-conserving two-dimensional formulation for compressible, piezoviscous and non-Newtonian fluids, *Tribol. Int.* **67**, 61 (2013).
- [42] F. Mezzadri and E. Galligani, An inexact Newton method for solving complementarity problems in hydrodynamic lubrication, *Calcolo* **55**, 1 (2018).
- [43] K. L. Johnson, J. A. Greenwood, and S. Y. Poon, A simple theory of asperity contact in elastohydro-dynamic lubrication, *Wear* **19**, 91 (1972).
- [44] R. Gohar and H. Rahnejat, *Fundamentals of Tribology* (Imperial College Press, London, UK, 2008).
- [45] M. H. Müser, *et al.*, Meeting the contact-mechanics challenge, *Tribol. Lett.* **65**, 118 (2017).
- [46] W. B. Dapp, A. Lücke, B. N. J. Persson, and M. H. Müser, Self-Affine Elastic Contacts: Percolation and Leakage, *Phys. Rev. Lett.* **108**, 244301 (2012).
- [47] J. A. Greenwood and J. J. Wu, Surface Roughness and Contact: An Apology, (n.d.).
- [48] C. Campañá and M. H. Müser, Practical Green's function approach to the simulation of elastic semi-infinite solids, *Phys. Rev. B* **74**, 075420 (2006).
- [49] R. I. Taylor, Rough surface contact modelling—a review, *Lubricants* **10**, 5 (2022).
- [50] B. J. Hamrock, S. R. Schmid, and B. O. Jacobson, *Fundamentals of Fluid Film Lubrication*, 2nd ed. (CRC Press, Boca Raton, 2004).
- [51] A. Silva, V. Lenzi, A. Cavaleiro, S. Carvalho, and L. Marques, FELINE: Finite element solver for hydrodynamic lubrication problems using the inexact Newton method, *Comput. Phys. Commun.* **279**, 108440 (2022).
- [52] K. He, X. Zhang, S. Ren, and J. Sun, in *2015 IEEE International Conference on Computer Vision (ICCV)* (2015), pp. 1026–1034.
- [53] M. Capra, B. Bussolino, A. Marchisio, G. Masera, M. Martina, and M. Shafique, Hardware and software optimizations for accelerating deep neural networks: Survey of current trends, challenges, and the road ahead, *IEEE Access* **8**, 225134 (2020).
- [54] A. F. Agarap, Deep Learning Using Rectified Linear Units (ReLU), [arXiv:1803.08375](https://arxiv.org/abs/1803.08375).
- [55] L. Lu, Y. Shin, Y. Su, and G. E. Karniadakis, Dying ReLU and initialization: Theory and numerical examples, *Commun. Comput. Phys.* **28**, 1671 (2020).
- [56] S. J. Reddi, S. Kale, and S. Kumar, On the Convergence of Adam and Beyond, [arXiv:1904.09237](https://arxiv.org/abs/1904.09237).
- [57] S. Salman and X. Liu, Overfitting Mechanism and Avoidance in Deep Neural Networks, [arXiv:1901.06566](https://arxiv.org/abs/1901.06566).
- [58] H. H. Tan and K. H. Lim, in *2019 7th International Conference on Smart Computing & Communications (ICSCC)* (IEEE, Sarawak, Malaysia, Malaysia, 2019), pp. 1–4.
- [59] Keras: Deep Learning for Humans, www.keras.io (2023).
- [60] M. Abadi, *et al.*, TensorFlow: Large-Scale Machine Learning on Heterogeneous Distributed Systems, [arXiv:1603.04467](https://arxiv.org/abs/1603.04467).
- [61] F. Pedregosa, *et al.*, Scikit-learn: Machine learning in PYTHON, *J. Mach. Learn. Res.* **12**, 2825 (2011).
- [62] J. Hansen, M. Björling, and R. Larsson, Lubricant film formation in rough surface non-conformal conjunctions subjected to GPa pressures and high slide-to-roll ratios, *Sci. Rep.* **10**, 1 (2020).
- [63] C. A. R. Hoare, Algorithm 64: Quicksort, *Commun. ACM* **4**, 321 (1961).
- [64] N. Tala-Ighil, M. Fillon, and P. Maspeyrot, Effect of textured area on the performances of a hydrodynamic journal bearing, *Tribol. Int.* **44**, 211 (2011).
- [65] <https://doi.org/10.34622/datarepositorium/MUVOJD>